Journal of Alloys and Compounds 680 (2016) 406–414

Contents lists available at ScienceDirect

Journal of Alloys and Compounds

journal homepage: http://www.elsevier.com/locate/jalcom

# Mesoporous $SiO_2$ yolk shell confined core-satellite Ag nanoparticles: Preparation and catalytic activity

Ya Mao [a], Wanquan Jiang [a, *], Sheng Wang [a], Mei Liu [a], Shouhu Xuan [b, **], Xinglong Gong [b, ***], Ken Cham-Fai Leung [c]

[a] Department of Chemistry, University of Science and Technology of China (USTC), Hefei, 230026, PR China
[b] CAS Key Laboratory of Mechanical Behavior and Design of Materials, Department of Modern Mechanics, USTC, Hefei, 230027, PR China
[c] Department of Chemistry and Institute of Creativity, Hong Kong Baptist University, Kowloon, Hong Kong, China

ARTICLE INFO

*Article history:*
Received 23 December 2015
Received in revised form
5 March 2016
Accepted 14 April 2016
Available online 16 April 2016

*Keywords:*
Mesoporous
Yolk-shell
Ag@mSiO$_2$
Nanosphere
Catalysts
Recyclability

ABSTRACT

In this work, novel mesoporous $SiO_2$ yolk-shell confined core-satellite Ag nanoparticles (Ag@mSiO$_2$) synthesized with a simple route were reported. Firstly, the core/shell Ag@C nanospheres whose carbon shells were doped with Ag nanoparticles, were facilely prepared by using a simple hydrothermal method. After coating with a uniform layer of hybrid $SiO_2$ in the presence of octadecyltrimethoxysilane ($C_{18}$TMS), the Ag@C@h-$SiO_2$ composite nanospheres were obtained. The final calcination removed all the carbon and organic compound and left the yolk shell Ag@mSiO$_2$ nanosphere, in which an individually large Ag core and many tiny Ag nanoparticles were encapsulated within the mesoporous silica shell. The core-satellite like Ag nanoparticles exhibited excellent catalytic activity in RhB reduction. Benefited from the *m*-$SiO_2$ shell with a uniform pore size of 3.5 nm, the bi-mode Ag nanoparticles were very stable, thus the activity of Ag@mSiO$_2$ could keep as high as 92% after five cycles.



## 1. Introduction

Recently, much efforts have been made to design and fabricate nanomaterials with different morphologies and compositions, aiming for exploring the desired materials which can provide powerful platforms for nanocatalysis [1], nanoreactor [2], controlled drug release [3], sterilization [4], energy storage and conversion [5], water treatment [6], and so on [7] and [8]. Particularly, the mesoporous yolk-shell nanoparticles (MYSNs), a special class of core-shell structure with a distinctive core@void@shell configuration, with the distinctively movable cores, interstitial hollow spaces, and the functionalized mesoporous shells have attracted more and more attention for a variety of applications such as lithium-ion batteries [9], catalysis [10], biosensors [11], drug/gene delivery [12] and [13], and surface-enhanced Raman scattering [14], and so on [15] and [16]. Ever since the first demonstration of yolk-shell Au@mesoporous polymer shell and carbon shell by Hyeon et al. [17], a large number of MYSNs with different core and shell compositions and in wide range of particle sizes, shapes, and structures have been successfully synthesized, characterized and utilized in key promising applications, including metal@silica [18], metal oxide@silica [19], metal@carbon [20], metal oxide@carbon [21], metal@metal oxide [22], metal oxide@-metal oxide [23], metal@polymer [17], and so on. The original intent of the encapsulation is to protect the core so that its functionality will not be diminished upon aggregation or sintering under hash reaction conditions, or through interaction with surrounding environment [24] and [25].

Many researchers in this area are devoted to developing new synthetic strategies involving fewer preparing steps for the MYSNs with different components and shell structures. One of the general approaches is a template-assisted selective removal in which the core is coated with double shells consisting of different materials. The interlayer can be removed by a solvent etching or calcination [26] and [27], leaving a huge cavity. The mesopores in the outer layer which distinctly divided into ordered mesopores and disordered mesopores can be obtained by removal of the pore-making agent through calcination or solvent etching. For example, silane

* Corresponding author.
** Corresponding author.
*** Corresponding author.
*E-mail addresses:* jiangwq@ustc.edu.cn (W. Jiang), xuansh@ustc.edu.cn (S. Xuan), gongxl@ustc.edu.cn (X. Gong).

http://dx.doi.org/10.1016/j.jallcom.2016.04.139
0925-8388/

coupling agent such as $C_{18}$TMS is a kind of pore-making agent for disordered mesopores [28], and cationic surfactant such as CTAB and nonionic surfactant $F_{123}$ are contributed to the ordered mesopores' formation [29] and [30].

Mesoporous silica has emerged as one of the most promising mesoporous nanomaterials owing to its outstanding peculiarities, such as facile synthesis, tunable pore and particle size, good mechanical and thermal stability, easy modification, low toxicity, high biocompatibility, excellent affinity with other materials, and extended capacity of loading guest species [31] and [32]. Ag nanoparticles have acquired more and more interest due to their relatively cheap sources, high antibacterial activity against a wide range of bacteria and viruses, and excellent catalytic properties in many chemical reactions [33] and [34]. However, the rational combination of two or more different components together to give novel multifunctional materials with elevated practical performances remains a great challenge. Up to now, few reports have mentioned the mesoporous yolk-shell Ag@m$SiO_2$ nanocomposite, even fewer have involved about the mesoporous $SiO_2$ yolk shell confined core-satellite Ag nanoparticles. Therefore, the demand of exploring mesoporous yolk-shell Ag@m$SiO_2$ nanocatalysts with higher efficiency and preferable recyclability has driven the development of our target MYSNs.

In this article, a general strategy for the synthesis of yolk-shell nanospheres of an individually large Ag core and many tiny Ag nanoparticles were encapsulated within a mesoporous silica shell was reported for the first time. As depicted in Scheme 1, firstly, the core-shell Ag@C nanospheres with plenty of Ag nanoparticles confined in the carbon shells were easily synthesized through sonication-assisted hydrothermal treatment. Then the core-shell Ag@C nanospheres were facilely encapsulated by a uniform layer of h-$SiO_2$ via classical Stöber method after the treatment with PVP, employing a molar ration of TEOS/$C_{18}$TMS = 4.7. Finally, the yolk shell Ag@m$SiO_2$ nanosphere, in which an individually large Ag core and many tiny Ag nanoparticles were encapsulated within the mesoporous silica shell formed after the Ag@C@h-$SiO_2$ endured a high-temperature calcination to fully remove the carbon interlayer and the pore-making agent $C_{18}$TMS. It was noted that, the original Ag nanoparticles lurked in the carbon shell of Ag@C gradually grew up with each preparing step proceeding, entered into the mesopores during the calcination, and forming a novel kind of mesoporous $SiO_2$ confined core-satellite Ag nanoparticles. The resultant disordered pores in $SiO_2$ shell have a uniform size of 3.5 nm, which is smaller than the size of tiny Ag nanoparticles in the Ag@m$SiO_2$, so as to protect the Ag nanoparticles from leaching out. The unique Ag@m$SiO_2$ nanospheres are highly active in the reduction of RhB with $NaBH_4$ as the reductant, and the catalysts could be facilely recycled 5 times without obvious deterioration in activity. Moreover, Pal et al. [35]. reported that with decrease in size of noble metal nanoparticles, the activation energy decreases, leading to higher reaction rate. It is reasonably believed that the excellent catalytic activation mainly comes from the tiny Ag nanoparticles. In addition, the porous shell allows chemical and biological molecules to adhere to the surface of the large Ag core and the tiny Ag nanoparticles for more applications in catalysis and biomedical fields.

## 2. Experimental section

### 2.1. Materials

Silver nitrate ($AgNO_3$), L-ascorbic acid ($C_6H_8O_6$), hexadecyl trimethyl ammonium Bromide (CTAB), polyvinylpyrrolidone (PVP, 30 kDa), tetraethoxysilane (TEOS), octadecyltrimethoxysilane ($C_{18}$TMS), ammonia hydroxide ($NH_4OH$), ethanol (EtOH), sodium tetrahydridoborate ($NaBH_4$), Rhodamine *B* dye (RhB), and other reagents were bought from Sinopharm Chemical Reagent Co. Lt., (SCRC). They were of analytical grade and used without further purification. Deionized water was used in the whole experiments.

### 2.2. Procedure for the preparation of mesoporous $SiO_2$ yolk-shell confined core-satellite Ag nanocomposite Ag@m$SiO_2$

(1) Preparation of Ag@C core-shell nanoparticles

Ag@C core-shell nanoparticles were synthesized in accordance with the modified reported method [36]. Typically, $AgNO_3$ (0.1698 g) and CTAB (0.1093 g) were dissolved in 30 mL $H_2O$ under sonication, then ascorbic acid aqueous solution (0.03522 g/mL, 10 mL) was added slowly with an injection syringe, after sonication for 10 min, the mixture was sealed in a 50 mL Teflon-lined stainless-steel autoclave, and then transferred to an autoclave, the temperature was maintained at 160 °C for 24 h. The resultant olive-green suspension was isolated by centrifugation in water and ethanol, and then dried in vacuum for more than 6 h.

(2) Surface treatment of Ag@C with PVP

In order to be easily wrapped with amorphous silica, the Ag@C core-shell nanospheres were modified with PVP in advance. Specifically, 30 mg Ag@C and 150 mg PVP were dissolved in 120 mL ethanol, and then the mixture was stirred for 12 h under room temperature. The PVP modified Ag@C nanospheres were collected by centrifugation and redissolved in 20 mL ethanol.

(3) Encapsulation of Ag@C in amorphous h-$SiO_2$ shell

Amorphous silica was condensed on the surface of PVP modified Ag@C nanospheres by the classical Stöber method. The as-prepared 20 mL PVP modified Ag@C ethanol solution and 10 mL $H_2O$ were mixed with 100 mL isopropanol and 3 mL ammonium hydroxide under sonication, and then $C_{18}$TMS/TEOS (30 μL/75 μL) mixture was added dropwise with microsyringe under vigorous stirring. The reaction system was kept stirring under 30 °C for 6 h. The products

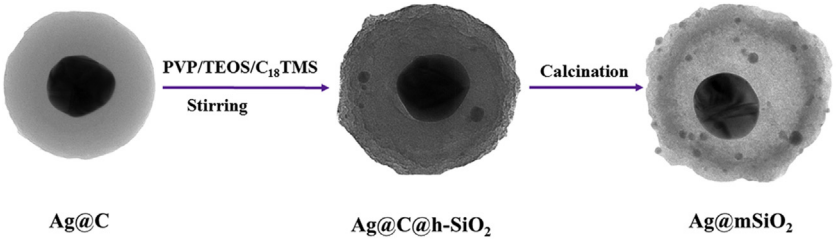


**Scheme 1.** Synthetic procedure of mesoporous $SiO_2$ yolk-shell confined core-satellite Ag nanoparticles Ag@m$SiO_2$.

were collected by centrifugation with water and ethanol, and then dried in vacuum for more than 6 h at 30 °C.

(4) Formation of mesoporous $SiO_2$ yolk-shell confined core-satellite Ag nanoparticles Ag@m$SiO_2$

The carbon interlayer and the pore-making agent $C_{18}$TMS were removed via a programmed heating muffle furnace in air atmosphere. The temperature was increased from room temperature to 550 °C with the heating rate was 5 °C/min, and the samples were treated at 550 °C for 5 h.

### 2.3. Catalytic application of Ag@m$SiO_2$ in RhB reduction

To investigate the catalytic activity of the target Ag@m$SiO_2$ nanocomposites, the reduction of RhB in the presence of $NaBH_4$ was chosen as the model reaction. Typically, RhB ($1.25 \times 10^{-5}$ mol/L, 10 mL) aqueous solution was mixed with a certain amount (60 μL, 80 μL, 100 μL) of Ag@m$SiO_2$ ethanol solution (5 mg/2 mL), with the addition of $NaBH_4$ (0.0038 g), the color of the bright red RhB solution vanished gradually, demonstrating the successful reduction of RhB. To investigate their recyclability, the Ag@m$SiO_2$ nanocomposites were recycled 5 times in accordance with the above method. The RhB ($1.25 \times 10^{-5}$ mol/L, 30 mL) aqueous solution was mixed with 250 μL of Ag@m$SiO_2$ ethanol solution (5 mg/2 mL). Then, the $NaBH_4$ (0.0114 g) was added and the reduction of RhB processed. After the reaction, the Ag@m$SiO_2$ was recovered by centrifugation.

### 2.4. Characterization

The crystal structures of the samples were obtained by X-ray powder diffraction patterns (XRD) in a Japan Rigaku DMax-γA rotating anode X-ray diffractometer using graphite monochromatized Cu Kα radiation (λ = 0.154178 nm). The field emission transmission electronic microscopy (FETEM) images of the samples were observed on a JEM-2100 F with an accelerating voltage of 200 kV. The field emission scanning electronic microscopy (FESEM) images were obtained on a JEOL JSM-6700 F SEM. The UV–vis absorption spectra of the samples were measured on a DUV-3700 UV-VIS-NIR Recording Spectrophotometer. The Raman spectra of the samples were obtained on a LABRAM-HR confocal laser microraman spectrometer. FTIR spectra of the samples in the wavenumber range 4000–400 $cm^{-1}$ were recorded on a TENSOR Model 27 Fourier transform infrared (FT-IR) spectrometer with KBr pellets. X-ray photoelectron spectra (XPS) of the samples were taken on an ESCALAB 250. Thermogravimetric (TG) analysis were performed on a DTG-60H thermogravimetric instrument, the samples were put in alumina pans at a heating rate of 10 °C/min to 700 °C in the atmosphere of air flowing at 50 mL/min. The Ag contents of the target products were determined by an Optima 7300DV inductive coupled plasma atomic emission spectrometer (ICP-AES). The UV–vis spectra during the catalyzed process of the reaction system were recorded on a TU-1901 spectrophotometer.

## 3. Results and discussion

### 3.1. Synthesis and characterization of mesoporous $SiO_2$ yolk-shell confined core-satellite Ag nanoparticles Ag@m$SiO_2$

Crystalline phases of the samples were investigated by X-ray powder diffraction (XRD). The reflection planes of (111), (200), (220) are observed in the three curves in Fig. 1, indicating a face-centered cubic structure of silver (JCPDS 04–0783) with calculated cell parameter a = 4.08 Å. No other peaks appeared finely

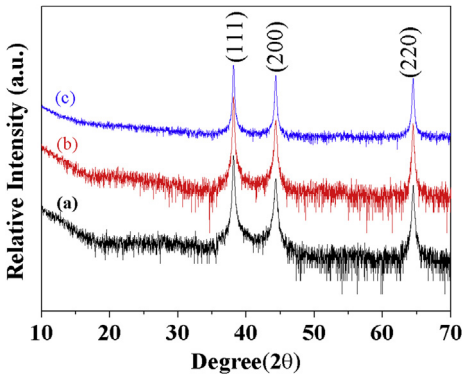


**Fig. 1.** XRD patterns of the as-synthesized products (a) Ag@C, (b) Ag@C@h-$SiO_2$, (c) Ag@m$SiO_2$.

echoes the high purity of Ag nanoparticles. A weak and broad band at 20–30° in 2θ showed in Fig. 1b can be assigned to the amphorous silica layer, indicating the successful encapsulation of h-$SiO_2$ on the carbon layer of Ag@C.

Fig. 2 shows the typical TEM and SEM images of the products synthesized in the sequential reactions. All the products show a spherical morphology, and they are free of surface cracks and intersphere adherence. As shown in Fig. 2a and Fig. 2d, each core-shell Ag@C nanosphere has an individually large Ag core, and a carbon shell with the thickness ranging from 35 to 45 nm. The diameter of Ag@C is about 130–170 nm. Although no clear Ag nanoparticles are clearly observed in the carbon shell, the successful reduction of RhB catalyzed by Ag@C (Fig. S1, ESI†) indicates the existence of Ag-related substance in the carbon shell, for the large Ag core within the thick carbon shell has poor catalytic capability [37]. In consideration of the reductant L-ascorbic acid was excessive and the reaction time was long enough in the preparing process, so the Ag-related substance is most probably Ag nanoparticles. From Fig. 2b and Fig. 2e, the well-defined Ag@C@h-$SiO_2$ with much rougher surface are well dispersed in the Cu grid without any conglomeration, and its diameter is about 240 nm. Most importantly, apparent tiny Ag nanoparticles in the carbon shells can be seen distinctly, which could further demonstrates the existence of Ag nanoparticles in the carbon shell of Ag@C composites. The Ag nanoparticles in the carbon shell gradually grew up during the silica coating process, and the maximum size of the tiny Ag nanoparticles is approximately 5 nm. It is reasonable to speculate that there were also some smaller Ag nanoparticles existed in the carbon shell after silica coating, however, they couldn't be detected in such condition. After the removal of the carbon interlayer and the pore-making agent $C_{18}$TMS in the hybrid silica shell of Ag@C@h-$SiO_2$ through high-temperature calcination, the mesoporous yolk-shell Ag@m$SiO_2$ nanospheres (Fig. 2c and Fig. 2e) were produced. Here, an individually large Ag core and many tiny Ag nanoparticles were encapsulated within the mesoporous silica shell. The emerging tiny Ag nanoparticles in the huge cave and mesoporous silica shell may cause from aggregating for those who locate closely under high-temperature calcination in air. The core-satellite like Ag nanoparticles without any aggregation would be much favored in their future applications because conglomeration of nanoparticles has been deemed as one of the main obstacles in the preparation. The TEM images of single Ag@C, Ag@C@h-$SiO_2$, Ag@m$SiO_2$ and the corresponding enlarged area were shown in Fig. S2, ESI†.

X-ray photoelectron spectroscopy (XPS) was utilized to characterize the surface elemental components of the as-prepared samples. As shown in Fig. 3a, the peak of $C_{1s}$ is attributed to the carbon

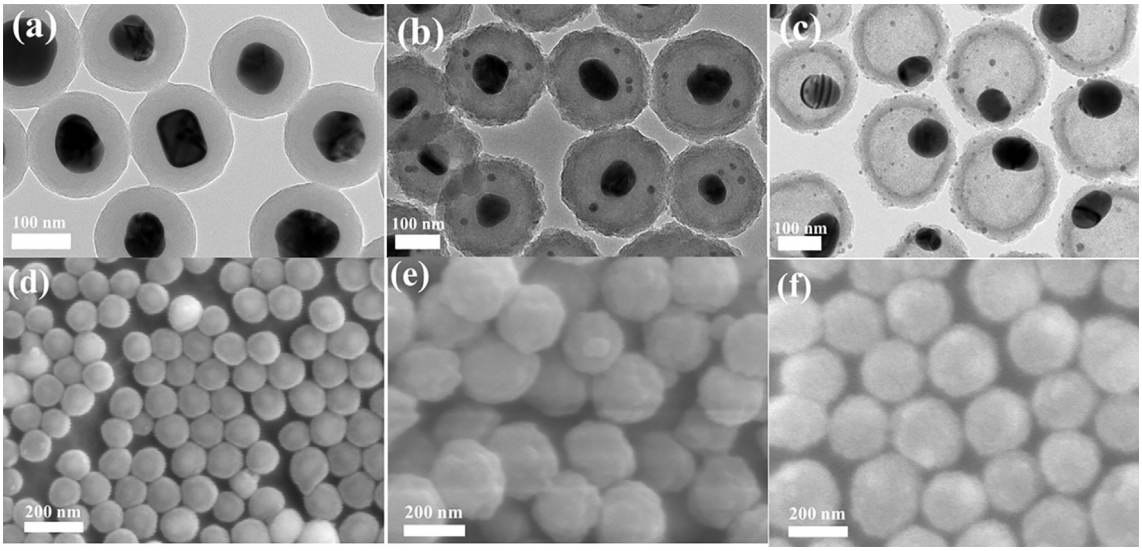


**Fig. 2.** TEM and SEM images of the as-synthesized products (a), (d) Ag@C; (b), (e) Ag@C@h-$SiO_2$; (c), (f) Ag@m$SiO_2$.

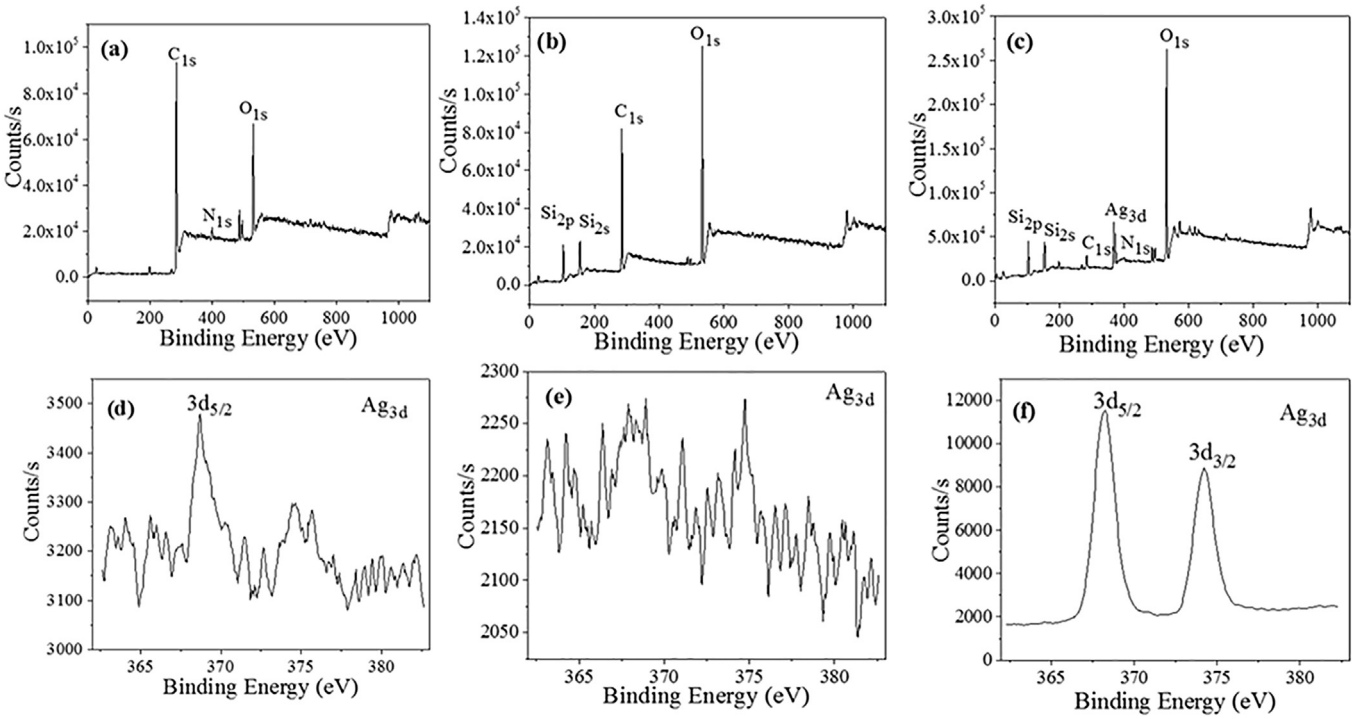


**Fig. 3.** XPS spectra of the as-synthesized products (a) Ag@C, (b) Ag@C@h-$SiO_2$, (c) Ag@m$SiO_2$. High-resolution Ag 3 d XPS spectra in (d) Ag@C, (e) Ag@C@h-$SiO_2$, (f) Ag@m$SiO_2$.

shell of Ag@C, the peak of $N_{1s}$ is derived from the residual of CTAB, and the peak of $O_{1s}$ is attributed to L-ascorbic and dehydroascorbic acid. From Fig. 3d, the binding energy at 368.75 eV corresponding to Ag $3d_{5/2}$ arises from elemental Ag in Ag@C can be detected with low intensity, the result is in good agreement of that the Ag cores are well confined into the carbon shells with the carbon shells are thicker than 10 nm, and there are Ag nanoparticles confined in the carbon shells. From Fig. 3b, the obvious peaks of $Si_{2s}$ and $Si_{2p}$, and the higher relative intensity of O to C compared with that in Ag@C, synchronously demonstrates the successful coating of h-$SiO_2$ on the surface of Ag@C. The thickness of the h-$SiO_2$ is about 40 nm, therefore, the peak of $Ag_{3d}$ in Ag@C@h-$SiO_2$ can't be detected (Fig. 3e). The distinct Ag $3d_{5/2}$ and $3d_{3/2}$ peaks shown in Fig. 3f responds to the existence of core-satellite Ag nanoparticles in the mesoporous yolk-shell Ag@m$SiO_2$, and the sharply increased relative intensity of O to C matches well with the complete removal of the carbon interlayer (Fig. 3c).

TGA was applied to verify the compositions of the as-prepared products. The whole weight loss process was performed from 25 to 700 °C. As shown in Fig. 4, the total weight loss of the Ag@C, Ag@C@h-$SiO_2$, and Ag@m$SiO_2$ are 57.34%, 56.03%, 3.47%, respectively. The minor differential of the weight loss between Ag@C and Ag@C@h-$SiO_2$ further confirms the thin thickness of silica on the surface of Ag@C, which matches well with the above TEM and SEM

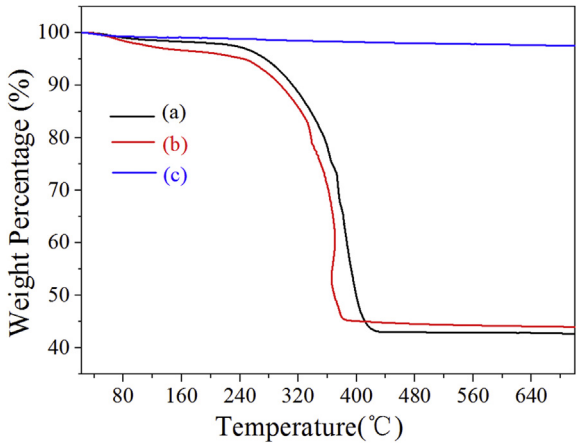


**Fig. 4.** TG curves of the as-synthesized products (a) Ag@C, (b) Ag@C@h-$SiO_2$, (c) Ag@m$SiO_2$.

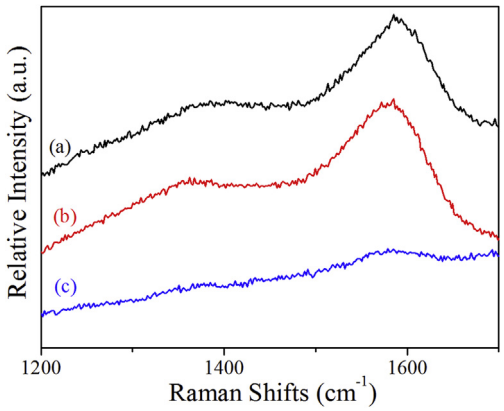


**Fig. 6.** Raman spectra of the as-synthesized samples (a) Ag@C, (b) Ag@C@h-$SiO_2$, (c) Ag@m$SiO_2$.

analysis. Meanwhile, on account of the incombustibility of $SiO_2$, the removal of $C_{18}$TMS could not compensate for the weight addition of $SiO_2$, so the weight loss of Ag@C@h-$SiO_2$ is merely a little lower than that of Ag@C. The nearly invariable weight of Ag@m$SiO_2$ during the weight loss process demonstrates the complete removal of carbon interlayer and pore-making agent $C_{18}$TMS in Ag@C@h-$SiO_2$ during the high-temperature calcination, which is crucial to the configuration of Ag@m$SiO_2$ and its catalytic properties.

Fig. 5 shows the FTIR spectra of the products synthesized in each step. The obvious absorption bands at 1620 $cm^{-1}$ and 1705 $cm^{-1}$ are attributed to the C=O vibrations, which are belong to the residual of L-ascorbic acid. The two distinctive peaks at 2854 $cm^{-1}$ and 2924 $cm^{-1}$ arise from *C*–H and C=O vibrations (Fig. 5b) are assigned to PVP, demonstrating the successful attachment of PVP to the carbon surface of Ag@C nanospheres. The strongest peak located at 1100 $cm^{-1}$ in Fig. 5b and Fig. 5c reveals the antisymmetric stretching vibration of *Si*–O, and corresponding to the successful h-$SiO_2$ coating. All the results indicate that the mesoporous $SiO_2$ yolk shell confined core-satellite Ag nanoparticles were successfully prepared.

As shown in Fig. 6a and Fig. 6b, the Raman bands at 1365 $cm^{-1}$ (D band) and 1587 $cm^{-1}$ (G band) are attributed to the two in-plane vibration modes of $sp^2$ *C*–C bonds in disordered carbon and crystalline graphitic carbon, respectively. The broad nature of the vibrational peaks indicates the low graphitization degree of the carbon shells, and the results clearly demonstrate the complete carbonization of L-ascorbic acid and dehydroascorbic acid during the hydrothermal synthesis. The relative intensity of G band to D band shown in Fig. 6c is much lower than that in Fig. 6a and Fig. 6b, indicating the sufficient calcination of the carbon shells, and thus forming the yolk-shell Ag@m$SiO_2$ nanospheres.

The UV–vis absorption spectra of the as-synthesized products dispersed in ethanol are displayed in Fig. 7. The absorption peak locates at 451 nm shown in Fig. 7a and Fig. 7b is corresponding to the plasma resonance of Ag nanoparticles. However, as shown in Fig. 7c, the maximum absorption of Ag@m$SiO_2$ shifts to 412 nm, the obvious blue-shift compared with Ag@C and Ag@C@h-$SiO_2$ is mainly due to the removal of carbon shells [38]. In consideration of the completely vanish of 585 nm peak absorption in Ag@m$SiO_2$ UV–vis absorption, it is reasonable to deduce that the peak absorption of 585 nm is caused by the amorphous carbon.

From Fig. 8a and Fig. 8b, the disordered but uniform pores in the silica shell of Ag@m$SiO_2$ could be clearly observed. The nitrogen adsorption–desorption isotherm curve and the corresponding Barret-Joyner-Halender pore size distribution curve of the as-synthesized Ag@m$SiO_2$ is shown in Fig. 8c. The isotherm exhibits a type IV characteristic with a distinct hysteresis loop in the $P/P_0$ range of 0.4–1.0, indicating the existence of uniform nanopores. The pore size distribution curve reveals that the Ag@m$SiO_2$ has a homogeneous pore size of 3–4 nm. Moreover, it is reasonable to deduce that the size of the tiny Ag nanoparticles in the mesoporous

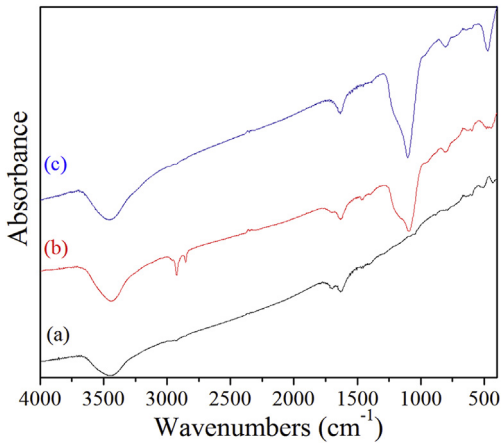


**Fig. 5.** FTIR spectra of the as-synthesized products (a) Ag@C, (b) Ag@C@h-$SiO_2$, (c) Ag@m$SiO_2$.

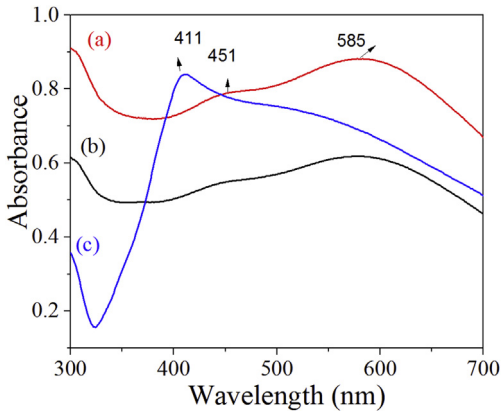


**Fig. 7.** UV–vis absorption spectra of the as-synthesized products (a) Ag@C, (b) Ag@C@h-$SiO_2$, (c) Ag@m$SiO_2$.

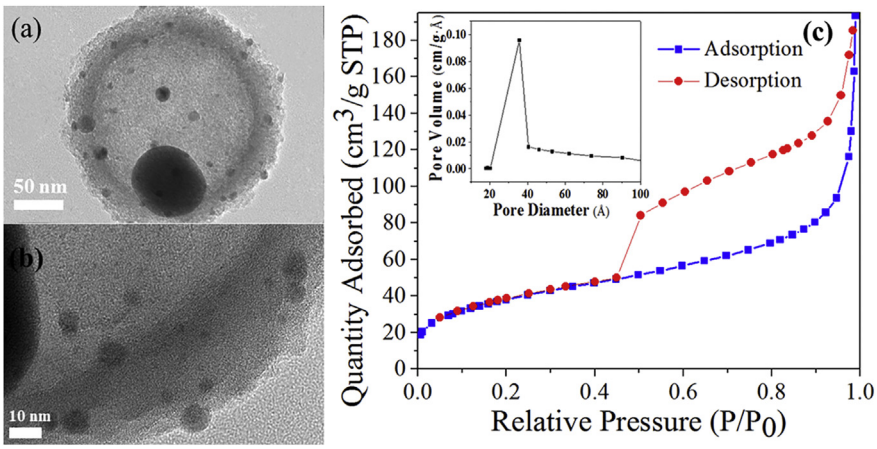


**Fig. 8.** (a) and (b) TEM images of the as-synthesized Ag@mSiO$_2$ nanosphere with different magnifications and (c) Nitrogen adsorption–desorption isotherm plot and pore size distribution curve (inset) of the Ag@mSiO$_2$.

SiO$_2$ shell and huge cavity is a little larger than that of nanopores in the silica shell, which is of crucial importance to the recyclability of Ag@mSiO$_2$.

### 3.2. *Plausible formation mechanism of mesoporous SiO$_2$ yolk shell confined core-satellite Ag nanoparticles Ag@mSiO$_2$*

A plausible formation mechanism of the mesoporous SiO$_2$ yolk shell confined core-satellite Ag nanoparticles Ag@mSiO$_2$. As illustrated in Fig. 9, in our typical synthesis of Ag nanoparticles decorated Ag@C core-shell nanospheres, CTAB may probably self-assemble into two kinds of micelles with different sizes under sonication, and well distributed in the aqueous solution. The mixture solution became bright yellow, indicating the formation of AgBr, and the AgBr confined in the micelles followed with a reduction reaction in the presence of L-ascorbic acid reductant, forming elemental Ag. Since L-ascorbic acid was excessive, it acted not only as a reductant, but also the resource of carbon layer. During the hydrothermal treatment process, the elemental Ag in the micelle restrict could aggregate into larger particles, and acted as seeds to induce the growth of carbon layer. Therefore, the carbonized L-ascorbic acid and dehydroascorbic acid clung to the preformed Ag nanoparticles, forming the Ag nanoparticles decorated Ag@C core-shell nanospheres.

The Ag@C nanospheres were pretreated with PVP for the successful silica coating. With a highly polar amide group in the pyrrolidone ring, the amphiphilic PVP can absorb on the surface of carbon shell, making it possible for carbon shell to be efficiently encapsulated by h-SiO$_2$. It has sufficient affinity of the carbon surface to the TEOS precursor, so as to restrain secondary nucleation of h-SiO$_2$ [39]. Notably, in the silica coating process, the Ag nanoparticles in the carbon shell of Ag@C nanosphere gradually grew up with the maximum size is about 5 nm. The nanoparticles gradually self-assembled into larger ones in the presence of PVP, for the size

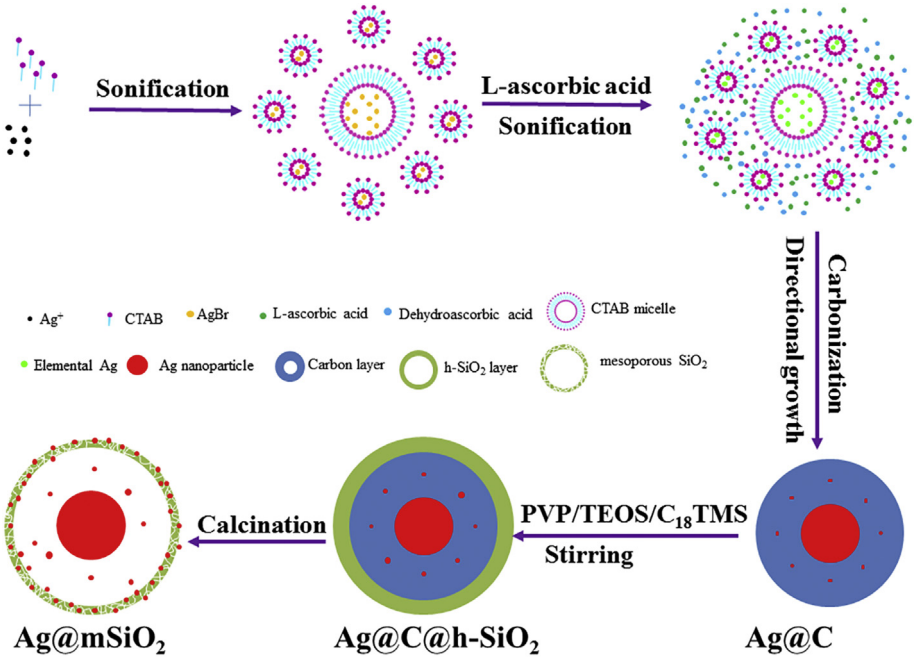


**Fig. 9.** Plausible formation mechanism of mesoporous yolk-shell Ag@mSiO$_2$ with mesoporous SiO$_2$ confined core-satellite Ag configuration.

of Ag nanoparticles could be adjusted to some extent by the use of PVP as a stabilizer. The residual $NO_3^-$ can interact with the Ag nanoparticles as well as pyrrolidone ring of PVP, that is the PVP-$NO_3^-$ polymer chains act as a soft binder for anchoring of Ag nanoparticles during the silica coating process [40] and [41].

In the calcination process, all the carbon and organic compound are removed, leaving the yolk shell Ag@m$SiO_2$ nanosphere with core-satellite Ag configuration, in which an individually large Ag core and many tiny Ag nanoparticles were encapsulated within the mesoporous silica shell. The tiny Ag nanoparticle whose size is smaller than the mesopores would enter into the disordered channel and the particles which locates closely would self-assembled into larger ones under high-temperature treatment. Therefore, the mesoporous silica with confined core-satellite Ag nanoparticles was obtained. The content of Ag in the Ag@m$SiO_2$ nanocomposite is 11.46%, which was measured by ICP-AES.

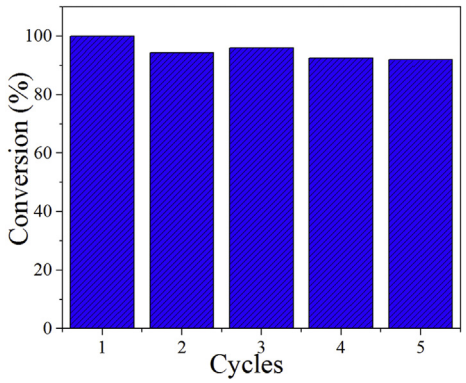


**Fig. 11.** Conversion of RhB in five successive cycles of reduction with Ag@m$SiO_2$.

### 3.3. Catalytic properties of the as-prepared Ag@m$SiO_2$ yolk-shell nanospheres

The reduction of RhB was chosen to evaluate the catalytic performance of Ag@m$SiO_2$, whereas the concentration change of RhB could be easily monitored by using a UV–vis absorption spectroscopy. No byproducts were formed. Here, the nanocatalyst is of great importance for the reduction reaction. According to the previous report [42], in the absence of nanocatalyst, the reduction of RhB proceeds very slowly that the RhB possesses only 30% conversion within 100 min with an excess of $NaBH_4$. Whereas, as soon as appropriate amount of Ag@m$SiO_2$ is added to the reaction system, the color of the reaction system changes gradually from pink to colorless. Fig. 10 shows the typical catalytic performance of the tiny Ag dotted mesoporous yolk-shell Ag@m$SiO_2$ nanospheres on the reduction of RhB. As shown in Fig. 10a, with increasing reaction time, the concentration of RhB decreases sharply, indicating a successful reduction catalyzed by Ag@m$SiO_2$. The reaction rate decreases slowly over time, which could be attributed to pseudo-first-order kinetics that had been reported before [43]. Meanwhile, the catalyzed reaction rate increases with increasing catalyst concentration (Fig. 10b). The recyclability of the Ag@m$SiO_2$ was also studied to evaluate their catalytic performance. As shown in Fig. 11, the conversion rate of RhB changes from 100% to 92% after five recycles, indicating the distinguished reusability of Ag@m$SiO_2$. In comparison to other reported Ag-based nanocatalysts such as Ag@$SiO_2$@Ag, Ag–$Fe_3O_4$@C, the unique mesoporous $SiO_2$ yolk shell confined core-satellite Ag nanoparticles Ag@m$SiO_2$ was synthesized in a much more simple route, and exhibited higher catalytic rate and superior recyclability, which could be ascribed to its unique morphology and excellent dispersity and homogeneity (Fig. 12). The huge cavity and the disordered mesopores in the $SiO_2$ shell provide a large space for the efficient loading of RhB, and the uniform 3–4 nm mesopores in the silica shell protect the tiny Ag nanoparticles from leaching. The sufficient contact of RhB with the tiny Ag nanoparticles brings up the excellent catalytic activity of Ag@m$SiO_2$. It is reasonable to believe that the distinguishingly catalytic activity mainly comes from the tiny Ag nanoparticles for the size-selective catalysis of noble metal [35].

## 4. Conclusions

In summary, the mesoporous $SiO_2$ yolk shell with confined core-satellite Ag nanoparticles Ag@m$SiO_2$ were successfully synthesized. Firstly, the Ag nanoparticles decorated Ag@C core-shell nanospheres were synthesized via a simple sonication-assisted hydrothermal method, followed with h-$SiO_2$ encapsulation with Stöber method to prepare the Ag@C@h-$SiO_2$, and high-temperature calcination to remove the carbon interlayer and the pore-making agent $C_{18}$TMS to form the target products with an individually large Ag core and many tiny Ag nanoparticles confined in the mesoporous $SiO_2$ shell. The Ag nanoparticles gradually grow up during the silica coating and high-temperature calcination process, safely reside in the huge cavity and the mesopores of silica shell due

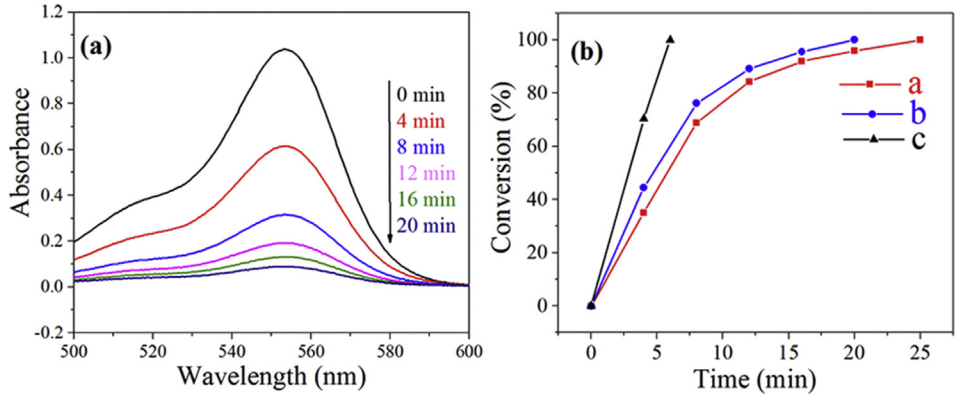


**Fig. 10.** (a) UV–vis spectra of the reduction of RhB during the reduction catalyzed by Ag@m$SiO_2$ nanocomposites. $[RhB]_0 = 1.25 \times 10^{-5}$ mol/L, $[NaBH_4]_0 = 1 \times 10^{-2}$ mol/L, $[Ag]_0 = 1.06 \times 10^{-5}$ mol/L. The arrow marks the increase of reaction time, showing the gradual reduction of RhB with Ag@m$SiO_2$ catalysts. (b) Plot of conversion (%) of RhB versus time (t, min) at different concentrations of Ag nanocatalyst (a) $[Ag]_0 = 7.95 \times 10^{-6}$ mol/L, (b) $[Ag]_0 = 1.06 \times 10^{-5}$ mol/L, (c) $[Ag]_0 = 1.32 \times 10^{-5}$ mol/L $[RhB]_0 = 1.25 \times 10^{-5}$ mol/L and $[NaBH_4]_0 = 1 \times 10^{-2}$ mol/L keep constant.

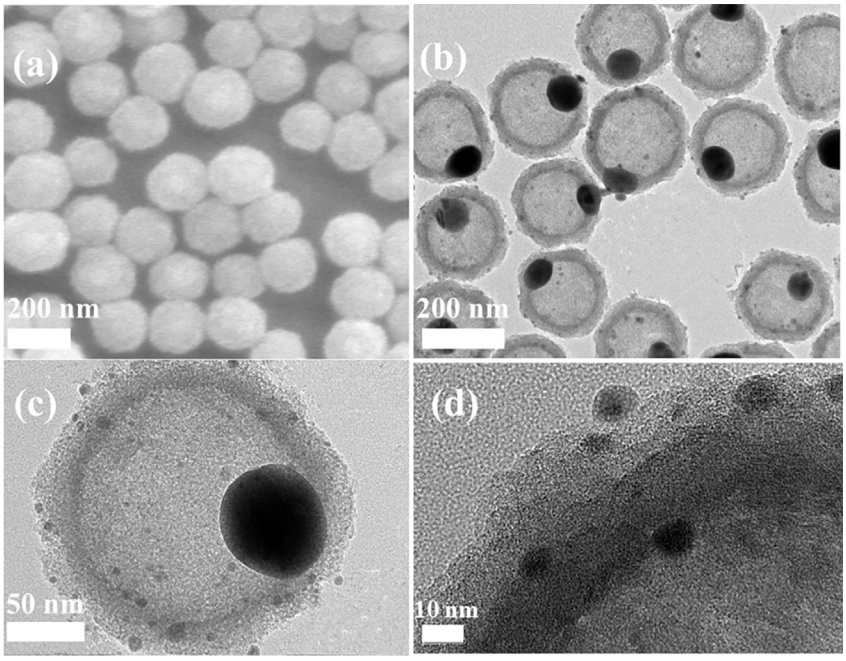


**Fig. 12.** (a) SEM and (b), (c), (d) TEM images of Ag@mSiO$_2$ with different magnifications.

to their diameter is a little larger than the size of mesopores in the silica shell. The mesoporous yolk-shell configuration of Ag@mSiO$_2$ nanocomposites provides a wonderful platform for the catalysis of RhB with ultra-fast catalytic rate and outstanding recyclability. Most importantly, these results offer a simple approach to construct mesoporous yolk-shell nanocomposites with nanocatalysts stably confined in the mesopores and cavity, which would endow wide applications in catalysis, energy storage, and other aspects.

## Acknowledgement

Financial supports from the National Natural Science Foundation of China (Grant No. 11372301), and HKRGC-GRF (201412 and 201213), are gratefully acknowledged. This work was also supported by Collaborative Innovation Center of Suzhou Nano Science and Technology.

## Appendix A. Supplementary data

Supplementary data related to this article can be found at http://dx.doi.org/10.1016/j.jallcom.2016.04.139.

## References

[1] T. Shen, M. Chen, C. Du, Y. Sun, Q. Tan, L. Du, G. Chen, G. Yin, Facile synthesis of $Pt_3Ni$ alloy nanourchins by temperature modulation and their enhanced electrocatalytic properties, J. Alloys Comp. 645 (2015) 309–316.
[2] Z. Chen, Z.-M. Cui, F. Niu, L. Jiang, W.-G. Song, Pd nanoparticles in silica hollow spheres with mesoporous walls: a nanoreactor with extremely high activity, Chem. Commun. 46 (2010) 6524–6526.
[3] J. Liu, W. Bu, L. Pan, J. Shi, NIR-triggered anticancer drug delivery by upconverting nanoparticles with integrated azobenzene-modified mesoporous silica, Angew. Chem. Int. Ed. 52 (2013) 4375–4379.
[4] M.A. Vetten, C.S. Yah, T. Singh, M. Gulumian, Challenges facing sterilization and depyrogenation of nanoparticles: effects on structural stability and biomedical applications, Nanomed. Nanotechnol. Biol. Med. 10 (2014) 1391–1399.
[5] D. Cai, D. Li, S. Wang, X. Zhu, W. Yang, S. Zhang, H. Wang, High rate capability of $TiO_2$/nitrogen-doped graphene nanocomposite as an anode material for lithium-ion batteries, J. Alloys Comp. 561 (2013) 54–58.
[6] J. Fu, J. Zheng, W. Fang, C. Chen, C. Cheng, R. Yan, S. Huang, C. Wang, Synthesis of porous magnetic $Fe_3O_4$/Fe@ZnO coree shell heterostructure with superior capability for water treatment, J. Alloys Comp. 650 (2015) 463–469.
[7] G.L. Li, H. Möhwald, D.G. Shchukin, Precipitation polymerization for fabrication of complex core-shell hybrid particles and hollow structures, Chem. Soc. Rev. 42 (2013) 3628–3646.
[8] N. Liu, X. Chen, Z. Ma, Ionic liquid functionalized graphene/Au nanocomposites and its application for electrochemical immunosensor, Biosens. Bioelectron. 48 (2013) 33–38.
[9] Q. Xie, X. Zhang, X. Wu, H. Wu, X. Liu, G. Yue, Y. Yang, D. Peng, Yolk-shell ZnO-C microspheres with enhanced electrochemical performance as anode material for lithium ion batteries, Electrochimica Acta 125 (2014) 659–665.
[10] Y. Sun, L. Zhang, Y. Wang, P. Chen, S. Xin, H. Jiu, J. Liu, Hollow and hollow core/shell $CeO_2/SiO_2$ @$CeO_2$ spheres: synthesis, structure evolution and catalytic properties, J. Alloys Comp. 586 (2014) 441–447.
[11] A. Guo, Y. Li, W. Cao, X. Meng, D. Wu, Q. Wei, B. Du, An electrochemical immunosensor for ultrasensitive detection of carbohydrate antigen 199 based on Au@Cu x OS yolk –shell nanostructures with porous shells as labels, Biosens. Bioelectron. 63 (2015) 39–46.
[12] Y.-M. Zhou, H.-B. Wang, M. Gong, Z.-Y. Sun, K. Cheng, X.-K. Kong, Z. Guo, Q.-W. Chen, Yolk-type Au@Fe3O4@C nanospheres for drug delivery, MRI and two-photon fluorescence imaging, Dalton Trans. 42 (2013) 9906–9913.
[13] Y. Wang, H. Gu, Core-shell-type magnetic mesoporous silica nanocomposites for bioimaging and therapeutic agent delivery, Adv. Mater. 27 (2015) 576–585.
[14] M. Lin, Y. Wang, X. Sun, W. Wang, L. Chen, "Elastic" property of mesoporous silica shell: for dynamic surface enhanced Raman scattering ability monitoring of growing noble metal nanostructures via a simplified spatially confined growth method, ACS Appl. Mater. Interfaces 7 (2015) 7516–7525.
[15] J. Zheng, C. Cheng, R. Yan, W. Fang, C. Chen, H. Huai, C. Wang, Synthesis of yolk-shell magnetic magnesium silicate with tunable yolk morphology for removal of methylene blue in water, J. Alloys Comp. 596 (2014) 5–9.
[16] K. Guo, M. Li, X. Fang, L. Bai, M. Luoshan, F. Zhang, X. Zhao, Improved properties of dye-sensitized solar cells by multifunctional scattering layer of yolk-shell-like $TiO_2$ microspheres, J. Power Sources 264 (2014) 35–41.
[17] M. Kim, K. Sohn, H.B. Na, T. Hyeon, Synthesis of nanorattles composed of gold nanoparticles encapsulated in mesoporous carbon and polymer shells, Nano Lett. 2 (2002) 1383–1387.
[18] Y. Chen, Q. Wang, T. Wang, One-pot synthesis of M (M = Ag, Au)@$SiO_2$ yolk-shell structures via an organosilane-assisted method: preparation, formation mechanism and application in heterogeneous catalysis, Dalton Trans. 44 (2015) 8867–8875.
[19] L. Wu, Y. Yu, Y. Zhang, Y. Li, Y. Zhang, J. Zhi, Large scale fabrication of highly monodispersed rattle-type $TiO_2$@void@$SiO_2$ spheres via synthesis-cum-organization process, J. Colloid Interface Sci. 369 (2012) 179–183.
[20] C. Galeano, R. Güttel, M. Paul, P. Arnal, A.H. Lu, F. Schüth, Yolk-shell gold nanoparticles as model materials for support-effect studies in heterogeneous catalysis: Au, @C and Au, @$ZrO_2$ for CO oxidation as an example, Chem. Eur. J. 17 (2011) 8434–8439.
[21] H. Wan, H. Qin, Z. Xiong, W. Zhang, H. Zou, Facile synthesis of yolk-shell magnetic mesoporous carbon microspheres for efficient enrichment of low

abundance peptides, Nanoscale 5 (2013) 10936–10944.
[22] Z. Jiang, W. Wei, D. Mao, C. Chen, Y. Shi, X. Lv, J. Xie, Silver-loaded nitrogen-doped yolk-shell mesoporous $TiO_2$ hollow microspheres with enhanced visible light photocatalytic activity, Nanoscale 7 (2015) 784–797.
[23] X. Wang, Y. Wang, L. Yang, K. Wang, X. Lou, B. Cai, Template-free synthesis of homogeneous yolk-shell $TiO_2$ hierarchical microspheres for high performance lithium ion batteries, J. Power Sources 262 (2014) 72–78.
[24] P.M. Arnal, M. Comotti, F. Schüth, High-temperature-stable catalysts by hollow sphere encapsulation, Angew. Chem. 118 (2006) 8404–8407.
[25] X. Fang, X. Zhao, W. Fang, C. Chen, N. Zheng, Self-templating synthesis of hollow mesoporous silica and their applications in catalysis and drug delivery, Nanoscale 5 (2013) 2205–2218.
[26] R. Liu, Y.-W. Yeh, V.H. Tam, F. Qu, N. Yao, R.D. Priestley, One-pot Stöber route yields template for Ag@carbon yolk–shell nanostructures, Chem. Commun. 50 (2014) 9056–9059.
[27] T. Yang, J. Liu, Y. Zheng, M.J. Monteiro, S.Z. Qiao, Facile fabrication of core-shell-structured Ag@Carbon and mesoporous yolk-shell-structured Ag@Carbon@Silica by an extended stöber method, Chem. Eur. J. 19 (2013) 6942–6945.
[28] J.C. Park, H. Song, Metal@Silica yolk-shell nanostructures as versatile bifunctional nanocatalysts, Nano Res. 4 (2011) 33–49.
[29] L. Zhang, T. Wang, L. Li, C. Wang, Z. Su, J. Li, Multifunctional fluorescent-magnetic polyethyleneimine functionalized $Fe_3O_4$-mesoporous silica yolk-shell nanocapsules for siRNA delivery, Chem. Commun. 48 (2012) 8706–8708.
[30] D. Li, J. He, W. Cheng, Y. Wu, Z. Hu, H. Tian, Y. Huang, Redox-responsive nanoreservoirs based on collagen end-capped mesoporous hydroxyapatite nanoparticles for targeted drug delivery, J. Mater. Chem. B 2 (2014) 6089–6096.
[31] X. Fang, X. Zhao, W. Fang, C. Chen, N. Zheng, Self-templating synthesis of hollow mesoporous silica and their applications in catalysis and drug delivery, Nanoscale 5 (2013) 2205–2218.
[32] R. Guillet-Nicolas, A. Popat, J.-L. Bridot, G. Monteith, S.Z. Qiao, F. Kleitz, pH-Responsive nutraceutical-mesoporous silica nanoconjugates with enhanced colloidal stability, Angew. Chem. 125 (2013) 2374–2378.
[33] R. Xiong, C. Lu, Y. Wang, Z. Zhou, X. Zhang, Nanofibrillated cellulose as the support and reductant for the facile synthesis of $Fe_3O_4$/Ag nanocomposites with catalytic and antibacterial activity, J. Mater. Chem. A 1 (2013) 14910–14918.
[34] M. Liong, B. France, K.A. Bradley, J.I. Zink, Antimicrobial activity of silver nanocrystals encapsulated in mesoporous silica nanoparticles, Adv. Mater. 21 (2009) 1684–1689.
[35] S. Panigrahi, S. Basu, S. Praharaj, S. Pande, S. Jana, A. Pal, S.K. Ghosh, T. Pal, Synthesis and size-selective catalysis by supported gold nanoparticles: study on heterogeneous and homogeneous catalytic process, J. Phys. Chem. C 111 (2007) 4596–4605.
[36] Z. Fang, K. Tang, S. Lei, T. Li, CTAB-assisted hydrothermal synthesis of Ag/C nanostructures, Nanotechnology 17 (2006) 3008–3011.
[37] S. Chen, Z. Wei, X. Qi, L. Dong, Y.G. Guo, L. Wan, L. Li, Nanostructured polyaniline-decorated Pt/C@PANI core-shell catalyst with enhanced durability and activity, J. Am. Chem. Soc. 134 (2012) 13252–13255.
[38] Y. Chen, Q. Wang, T. Wang, Fabrication of thermally stable and active bimetallic Au–Ag nanoparticles stabilized on inner wall of mesoporous silica shell, Dalton Trans. 42 (2013) 13940–13947.
[39] H. Yang, Y. Liu, Q. Shen, L. Chen, W. You, X. Wang, J. Sheng, Mesoporous silica microcapsule-supported Ag nanoparticles fabricated via nano-assembly and its antibacterial properties, J. Mater. Chem. 22 (2012) 24132–24138.
[40] C.L. Kuo, K.C. Hwang, Nitrate ion promoted formation of Ag nanowires in polyol processes: a new nanowire growth mechanism, Langmuir 28 (2012) 3722–3729.
[41] Q. Zhang, C.H. Moran, X. Xia, M. Rycenga, N. Li, Y. Xia, Synthesis of Ag nanobars in the presence of single-crystal seeds and a Bromide compound, and their surface-enhanced Raman scattering (sers) properties, Langmuir 28 (2012) 9047–9054.
[42] Y. Mao, W. Jiang, S. Xuan, Q. Fang, K.C.F. Leung, B.S. Ong, S. Wang, X.L. Gong, Rod-like β-FeOOH@poly(dopamine)-Au-poly(dopamine) nanocatalysts with improved recyclable activities, Dalton Trans. 44 (2015) 9538–9544.
[43] M. Zhu, C. Wang, D. Meng, G. Diao, In situ synthesis of silver nanostructures on magnetic $Fe_3O_4$@C core-shell nanocomposites and their application in catalytic reduction reactions, J. Mater. Chem. A 1 (2013) 2118–2125.